High Resolution AVO NMO

Jonathan E. Downton and Laurence R. Lines

ABSTRACT

This paper demonstrates a methodology to produce high-resolution AVO reflectivity attribute estimates similar to sparse spike deconvolution. Similar to poststack sparse deconvolution this reflectivity may be converted to impedance provided there are suitable additional constraints. The AVO estimate is performed prior to NMO avoiding the distortions and loss of frequency associated with this process. Long tailed *a priori* distributions are used to constrain the problem. The resulting sparse reflectivity is able to resolve thin layers and is more reliable than the estimates provided by the traditional AVO analysis that is performed on a sample-by-sample basis on NMO corrected gathers. This greater reliability is due to the classic trade-off between resolution and stability. With the new method a few sparse reflectivity values are estimated with greater certainty than the dense reflectivity at every time sample as in the traditional AVO analysis.

INTRODUCTION

We present a method for producing high-resolution estimates of AVO reflectivity attributes. The objective is to produce a sparse spike reflectivity series similar to that done by poststack sparse deconvolution (Levy and Fullagar, 1991; Sacchi, 1999; and Trad, 2002). Further, the methodology presented is analogous to the high-resolution Radon transform presented by Sacchi and Ulrych (1995). The new approach is better able to estimate reflectors undergoing NMO stretch and differential tuning than traditional AVO performed on a sample-by-sample basis on NMO corrected gathers. The inclusion of constraints and the waveform further stabilizes the inversion improving the reliability of the estimates compared with the traditional methodology. In addition, the approach provides a framework to estimate elastic impedances similar to poststack sparse spike impedance inversion.

The theory for this new algorithm is developed using a Bayesian formalism. Instead of the typical assumption of Gaussian probability distributions, various long-tailed distributions are used for the prior distribution. The likelihood model is based on the AVO NMO formalism (Downton and Lines, 2002) where the AVO and NMO inversions are performed simultaneously assuming some input wavelet. The inversion is nonlinear and must be solved using a bootstrap procedure. Conjugate gradient method is used to solve the inverse problem. Typically only a few iterations are needed to solve the problem so the algorithm is relatively quick.

Both synthetic seismic and real data examples are shown demonstrating the new methodology. The first example is constructed so as to illustrate how the new algorithm better estimates AVO reflectivity on events undergoing NMO stretch and tuning. The second example illustrates how the algorithm behaves on more realistic data created from well data. Real seismic data is used to show how the new algorithm gives more robust estimates in the presence of noise compared to the traditional method. Lastly the theory

needed to output impedances rather than reflectivity is developed and an example is shown illustrating the technique.

THEORY

Convolutional model

The convolutional model is used as the basis for the likelihood model. This model assumes the earth is composed of a series of flat, homogenous, isotropic layers. Ray tracing is done to map the relationship between the angle of incidence and offset. Transmission losses, converted waves, and multiples are not incorporated in this model and so must be addressed through prior processing. A modification of the two-term Fatti approximation (Fatti et al., 1994, Equation 4) is used to approximate the offset dependent reflectivity over some predefined angle range. Rather than solving for the P- and S-wave impedance reflectivity, we choose to solve for the P-wave impedance and fluid factor reflectivity since these two variables are uncorrelated.

The AVO NMO model (Downton and Lines, 2002) is the starting point for this inversion scheme. For the example of two offsets the AVO NMO formulation written in block matrix form is

$$\begin{bmatrix} \mathbf{d}_1 \\ \mathbf{d}_2 \end{bmatrix} = \begin{bmatrix} \mathbf{W}\mathbf{N}_1\mathbf{F}_1 & \mathbf{W}\mathbf{N}_1\mathbf{G}_1 \\ \mathbf{W}\mathbf{N}_2\mathbf{F}_2 & \mathbf{W}\mathbf{N}_2\mathbf{G}_2 \end{bmatrix} \begin{bmatrix} \mathbf{r}_P \\ \mathbf{r}_f \end{bmatrix}, \tag{1}$$

where **W** is a Toeplitz matrix representing the source wavelet, **N** is the NMO matrix describing the kinematics of the problem, **F** and **G** are diagonal matrices containing the weights as defined by the two term Fatti et al. (1994) equation. The column vectors $\mathbf{r}_p$, $\mathbf{r}_f$ describe the P-wave impedance and fluid factor reflectivity over some time interval. Likewise the column vectors $\mathbf{d}_1$, $\mathbf{d}_2$ represent the data at offset 1 and 2 over some time window. This formulation can be modified to include more offsets by just adding additional rows of block matrices to the problem. The NMO matrix **N** may be written to incorporate higher order NMO corrections or anisotropy, but the velocity must be specified *a priori*. Typically the analysis is performed over some limited angle range implying the data is muted. By incorporating NMO into the inverse problem, the NMO correction is never done as a processing step thus avoiding introducing NMO stretch distortions and biases. Differential tuning is incorporated as part of the forward model and so is dealt with.

This linear model described by Equation 1 can be written more simply as

$$\mathbf{d}=\mathbf{L}\mathbf{m}, \tag{2}$$

where **L** is the linear AVO NMO operator, **d** is the data vector and **m** is the unknown parameter vector describing the reflectivity. The data vector contains *N* time samples by *M* offsets while the parameter vector contains *2M* elements. This paper assumes the likelihood function is Gaussian for simplicity but it might be more appropriate for real seismic data to choose a robust distribution.

Prior model

Both the matrices **W** and **N** are typically underdetermined or ill-conditioned. This is due to the fact the data is band-limited and the differential tuning introduces null spaces into the **N** operator. Because of this, the problem needs to be regularized. This can be done by choosing a weighting function that will treat certain reflection coefficients as being more reliable than others. Choosing a long tailed *a priori* distribution will lead to such a weighting function.

A long tailed distribution or sparse reflectivity may be argued for based on physical arguments. The fluid factor reflectivity is sparse by its nature since it only responds to anomalous fluids or large changes in lithology. The P-wave impedance reflectivity may also be modeled as a long tailed distribution, such as the L1 distribution (Levy and Fullagar, 1981). Further, we make the typical assumption made in deconvolution that the reflectivity from different interfaces is uncorrelated so the resulting parameter covariance matrix is diagonal. Thus the two reflectivity series can be modeled by a variety of distributions including the Huber, Cauchy or Lp norm. Good results were obtained with each of these, but for illustration purposes this paper uses the Cauchy prior. Sacchi (1999) shows that this leads to a prior of the form

$$\frac{\partial J_q}{\partial m_j} = \mathbf{Qm}, \tag{3}$$

where J is the objective function and **Q** is a diagonal matrix that is defined as

$$Q_{kk} = \frac{1}{\sigma_p^2} \begin{cases} \dfrac{2}{\left(\dfrac{r_k^{\,2}}{2\sigma_p^2} + 1 \right)} & r_k \in r_p \\ \dfrac{\sigma_p^2}{\sigma_f^2} \dfrac{2}{\left(\dfrac{r_k^{\,2}}{2\sigma_f^2} + 1 \right)} & r_k \in r_f \end{cases}, \tag{4}$$

where σ_p and σ_f act in a similar fashion to the standard deviation of the P-wave impedance and fluid factor reflectivity. The weights are large when the reflectivity is small and small when the reflectivity is large. The matrix **Q** is estimated iteratively in a bootstrap fashion.

Nonlinear inversion

The Likelihood function (Equation 2) may be combined with the *a priori* probability function (Equation 3) using Bayes' theorem. There is no explicit interest in the variance of the time-domain constraints so it is marginalized (Sivia, 1996). The most likely solution can then be found by finding where the PDF is stationary. This involves taking the partial derivatives with respect to each parameter, setting the result to zero, and solving the set of simultaneous equations. This results in the nonlinear equation

$$\left[\mathbf{L}^{\mathrm{T}}\mathbf{L} + \mu\mathbf{Q}\right]\mathbf{m} = \mathbf{L}^{T}\mathbf{d}, \tag{5}$$

where $\mu = \boldsymbol{\varepsilon}^{T}\boldsymbol{\varepsilon}/(MN-1)$ and ***ε=Lm-d.*** There are two sources of nonlinearity in Equation (4), the estimate of the regularization parameter μ and the calculation of ***Q.***

The actual inverse problem being quite large, it is most efficiently solved using iterative techniques such as conjugate gradients (Skewchuk, 1994). Solving the inverse problem requires two nested loops. In the inner loop the conjugate gradient algorithm is used to solve Equation 5 using the previously calculated values of □ and Q. The maximum number of conjugate gradient iterations is used as a parameter to help stabilize the solution (Hansen, 1998). After solving for the reflectivity the estimate of □ and the covariance matrix Q is updated. Iteratively updating these parameters and re-estimating the reflectivity parameters constitute the outer loop. Generally a satisfactory sparse solution is obtained after 3 to 5 outer loops. For the first loop the inversion is run as an unconstrained inversion by setting □=0. Care must be taken in the first outer loop not to put too much detail in the solution or the problem will not converge. This can be controlled by carefully setting the maximum number of conjugate gradient iterations parameter to a value that limits resolution.

EXAMPLES

Synthetic example showing NMO stretch and differential tuning

To demonstrate that the new approach performs better in the presence of NMO stretch and differential tuning a synthetic model was created to demonstrate this. Dong (1999) quantified the error due to these two effects. Summarizing for the case of Ricker source wavelet, the intercept term *A* has approximately zero error while the gradient term *B,* after some rearrangement, has an error of the form

$$\frac{dB}{B} = \frac{\left(2\eta^{2}-1\right)\left(\eta^{2}-3\right)}{\left(2\eta^{2}-3\right)}\frac{A}{B}, \tag{6}$$

where $\eta = dt/f_0$ is defined in terms of the dominant frequency f_0 and the time interval *dt* of how far the time sample under investigation is from center of the wavelet. Thus the fractional error of the gradient is a function of η and the ratio of intercept over the gradient *A/B*. The leading term acts as scalar which is a function of η. The other factor which controls the size of the error is the ratio *A/B*. Thus it is possible to predict the size of the error for different classes of AVO anomalies as defined by Rutherford and Williams (1989). For a class I anomalies where $A<<B$ and a class II anomalies where $A\approx 0$ the expected error will be small. This is also true for most reflectors which fall along the mudrock trend since typically $A<<B$. However for class III and IV anomalies where $A>B$ the error will be potentially large. These predictions were tested and verified in Downton et al. (2003).

Based on this analysis a simple model was constructed which honored the assumption of sparse reflectivity, which had most of the reflectors following the mudrock trend and which had several class III and IV anomalies. These anomalies were created for both isolated and tuned reflectors. The synthetic data was generated using a convolutional model with a Ricker wavelet with a central frequency of 32.5 Hz central frequency. In order to isolate the affects of NMO stretch and differential tuning on the AVO inversion, the reflectivity was generated using the 3 term Shuey equation (1985) using the Gardner relationship to calculate density. By doing this the Smith and Gidlow (1987) AVO inversion could be used to perform the inversion exactly thus avoiding the introduction of theoretical error. Noise was added to give a signal-to-noise ratio of 4. A constant background velocity was used so there would be a simple angle to offset relationship. The maximum offset was chosen to be 4 times the target depth so that angles out to 65 degrees would be available for the inversion, though only angles to 45 degrees were actually used. These large angles were created to highlight the distortions. Figure 1 shows the generated prestack synthetic gather.

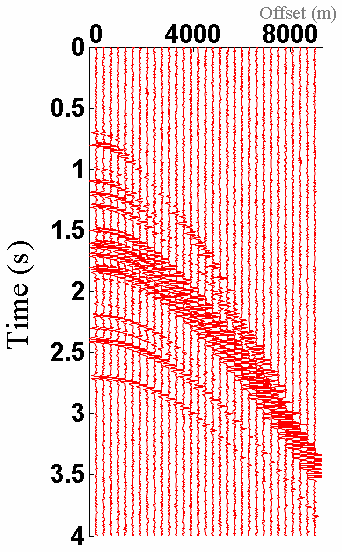

FIG. 1: Synthetic seismic gather. At zero offset and 1.5 sec. is the class III isolated reflector, at 1.6 s is the tuned class III reflector, at 1.7 s the isolated class IV anomaly and at 1.8 s the tuned class IV anomaly.

The middle panel of Figure 2 shows this gather after NMO correction. For comparison sake the same gather is shown that was generated without any moveout. Taking a difference between the two shows the theoretical error that is introduced by NMO stretch and differential tuning. This theoretical error will bias the AVO inversion.

An AVO inversion was performed using the Smith and Gidlow formulation using angles from 0 to 45 degrees. The Smith and Gidlow formulation was used rather than the 2-term Shuey approximation since the former is exact under the assumptions the model was created while the later is not. The reflectivity estimates where then transformed to intercept and gradient for display purposes as shown in Figure 3. As expected there is no error for the intercept term while the gradient term only shows error for both the class III and class IV anomalies. Reflectivity that falls along the mudrock trend is perfectly

predicted even though they undergo NMO stretch. Figure 3 also shows the reflectivity in the cross-plot domain. The class III and IV anomalies show significant scatter.

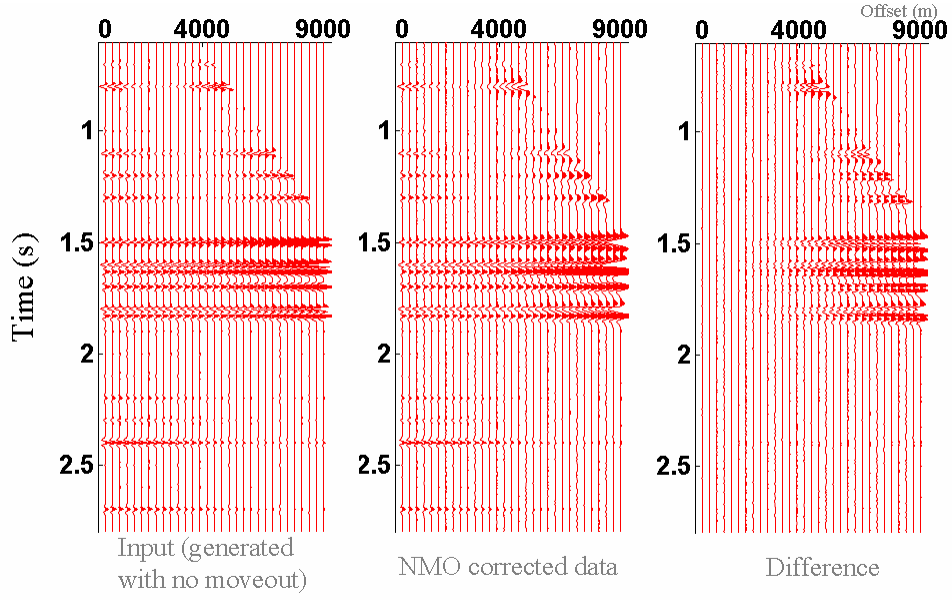

FIG. 2: The middle panel shows the NMO corrected gather from figure 1: The left panel shows the synthetic gather generated without moveout while the right panel shows the difference between the two.

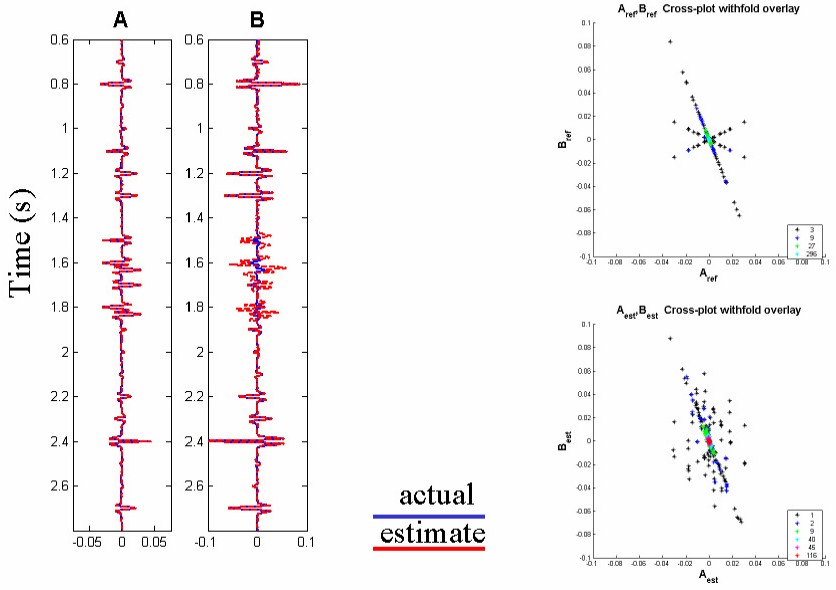

FIG. 3: The results of the traditional AVO inversion for intercept *A* and gradient *B*. The estimate is shown in red and the ideal in blue. This data is also shown in the cross-plot domain. The upper cross-plot is the ideal while the lower cross-plot is based on the estimate. Note the class III and IV anomalies are spread out in cross-plot space.

The same data was used to perform the high-resolution AVO NMO inversion. The results of this are shown in Figure 4 and 5. Figure 4 shows the input to the inversion, the estimated model reconstructed from the parameter estimates and the difference. The model matches the data closely with the difference only showing random noise. The estimated reflectivity is shown in figure 5. The estimate is now almost perfect for all reflectors including the class III and IV anomalies that were undergoing NMO stretch and had differential tuning. This is confirmed by cross-plotting the reflectivity.

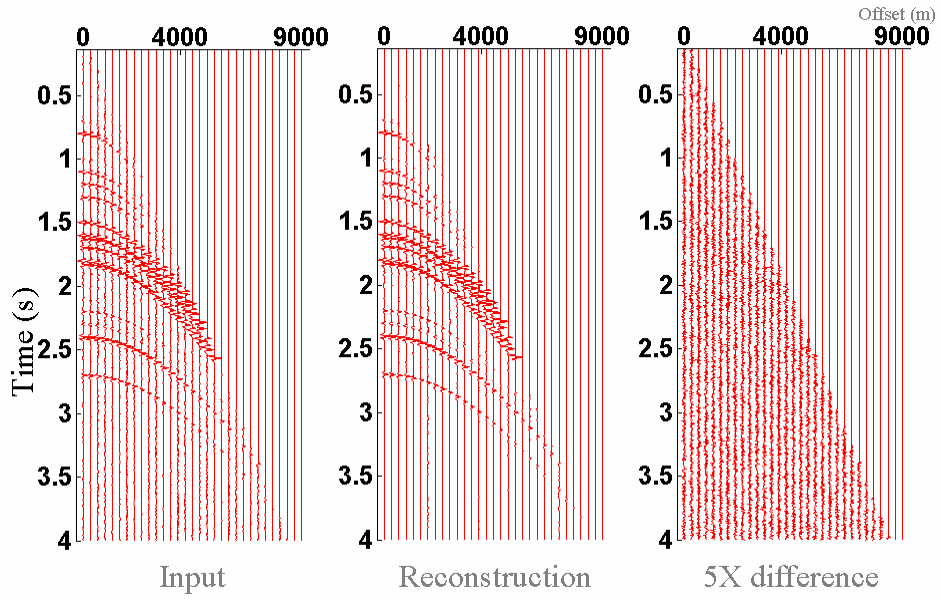

FIG. 4: Input to the AVO NMO inversion (left panel) and the model based on the AVO NMO inversion (middle panel). Note the good match between the two with only random noise showing up in the difference (right panel)

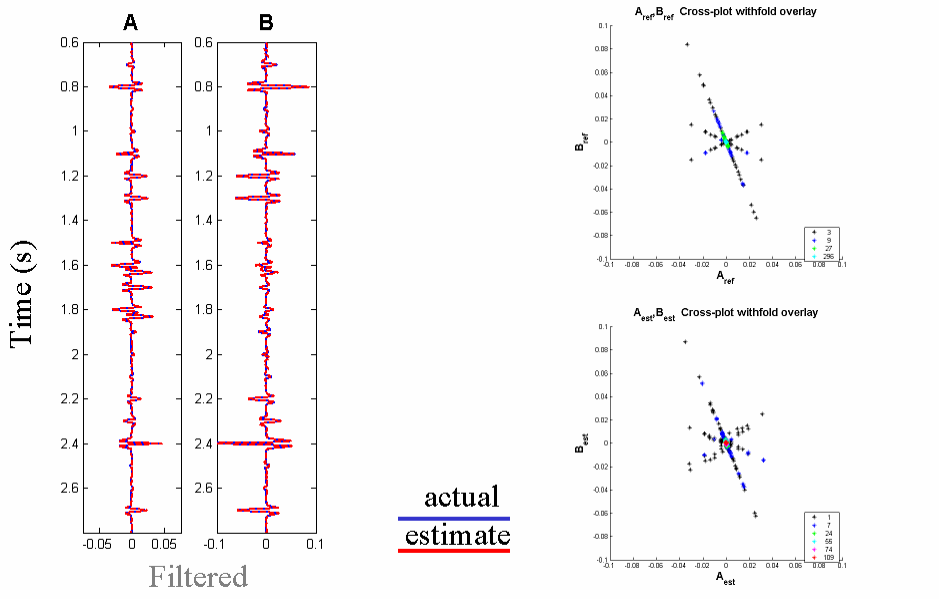

FIG. 5: The results of the high-resolution AVO NMO inversion for intercept *A* and gradient *B*. The estimate is shown in red and the ideal in blue. This data is also shown in the cross-plot domain. The upper cross-

plot is the ideal while the lower cross-plot is based on the estimate. Note the class III and IV anomalies are almost perfectly estimated now.

The AVO inversion estimates shown in Figure 5 are filtered with the source wavelet. Figure 6 shows the unfiltered reflectivity estimates shown in terms of the fluid factor, P- and S-wave impedance reflectivity. The match for the large reflectivity is almost perfect. With suitable modifications to the constraints to account for the background trend, these sparse spike reflectivity estimates may be used to estimate the P- and S-wave impedance as shown later in the paper.

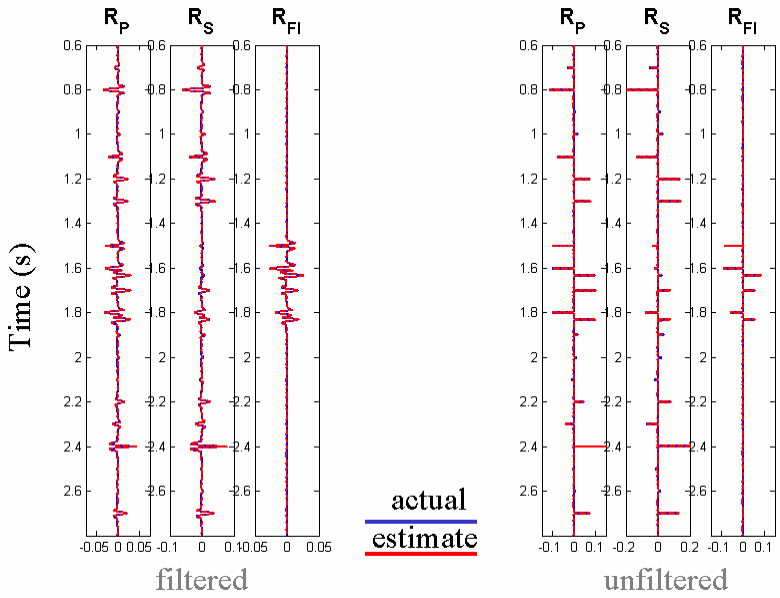

FIG. 6: Fluid factor, P- and S-wave impedance reflectivity estimates from the high-resolution AVO NMO inversion. The estimate is red and the ideal in blue. The left hand panel is filtered by the source wavelet while the right hand panel is the raw reflectivity estimate coming from the algorithm.

Synthetic data example based on well log

The preceeding example's input model was blocky and so the *a prior* assumptions were perfectly met. The next model tests what happens if the reflectivity does not match the *a priori* assumptions perfectly. For this second example the reflectivity is based on a well log from North Eastern British Columbia. The input well logs are shown in Figure 7 along with the synthetic seismic gather that was generated. In this case the reflectivity was generated with the Zoeppritz equation and convolved with a 10/14-90/110 Hz zero phase wavelet. Once again noise was added to give a signal-to-noise ratio of 4. The AVO inversion was done over angles from 0 to 35 degrees. The filtered estimate is close to perfect (Figure 8). The sparse spike reflectivity shows some errors particularly around 0.34 seconds on the S-wave impedance reflectivity.

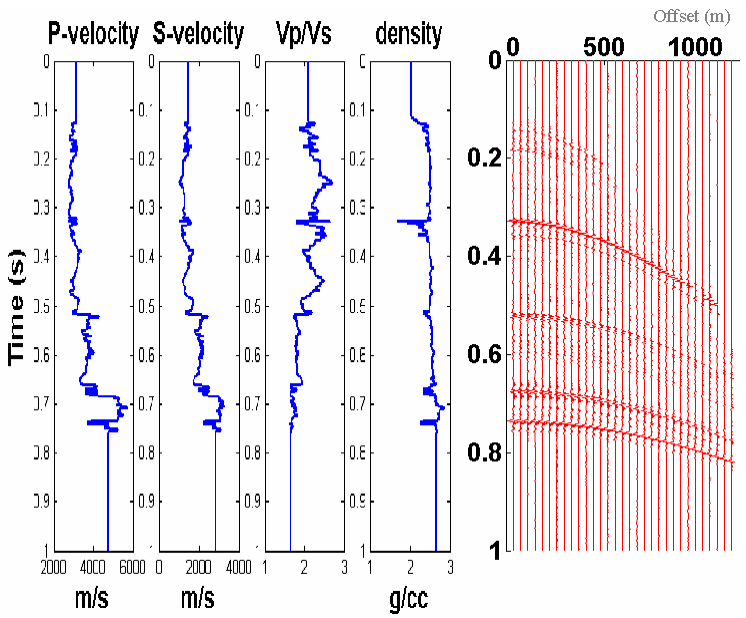

FIG. 7: Input density, P- and S-velocity logs used to generate synthetic gather shown at right

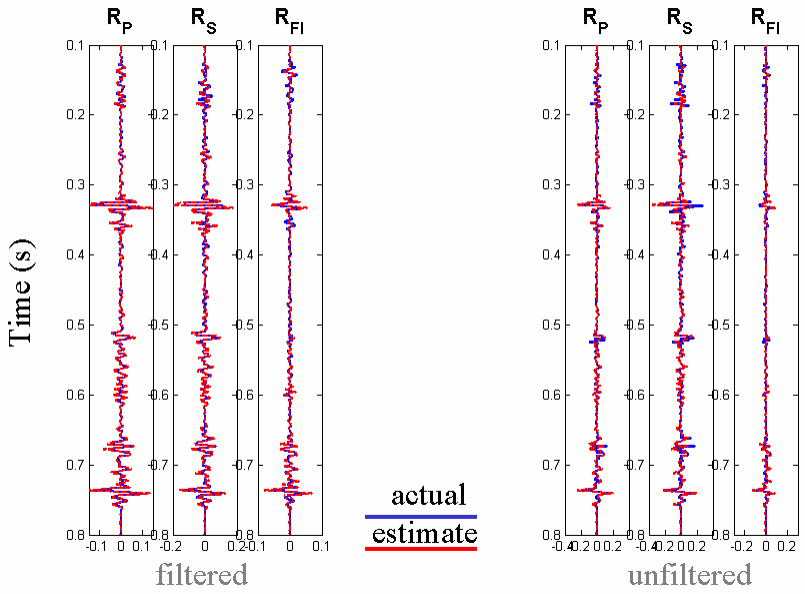

FIG. 8: Fluid factor, P- and S-wave impedance reflectivity estimates from the high-resolution AVO NMO inversion. The estimate is in red while the ideal is in blue. The filtered results (left panel) are almost perfect. The sparse spike estimate (right panel) is good with some problems on the S-wave impedance reflectivity.

Seismic data example

The seismic data example is from North East Saskatchewan. The well at shotpoint 3030 encountered two gas sands, an upper blanket sand and a channel sand. Both these gas sands should show fluid factor anomalies. The data has a good S/N ratio with signal extending from 10 to 130 Hz. The range of angles used in the in inversion was 0 to 36 degrees. The wavelet was calculated following Walden and White (1984).

Figure 9 shows the results of the high-resolution AVO NMO inversion. The bottom panel shows the fluid factor. The anomaly at 0.3 seconds is the top blanket sand and the anomaly at 0.4 seconds is the channel sand. The anomaly at 0.65 seconds with the peak over the trough represents a carbonate. In this case the fluid factor is responding to a change in lithology, which is off the mudrock trend. For comparison sake, Figure 10 shows the results from performing a traditional AVO inversion on NMO corrected gathers. Notice the significant improvement in S/N and continuity in the high-resolution AVO NMO inversion. This is probably due two factors. The fact the waveform is included in the formulation of the problem limits how quickly the filtered reflectivity can change temporally. Secondly, and probably more importantly the regularization of the problem improves the condition number of the problem decreasing how the noise gets amplified as part of the inversion. Figure 11 shows the prestack seismic data and the high resolution AVO NMO model.

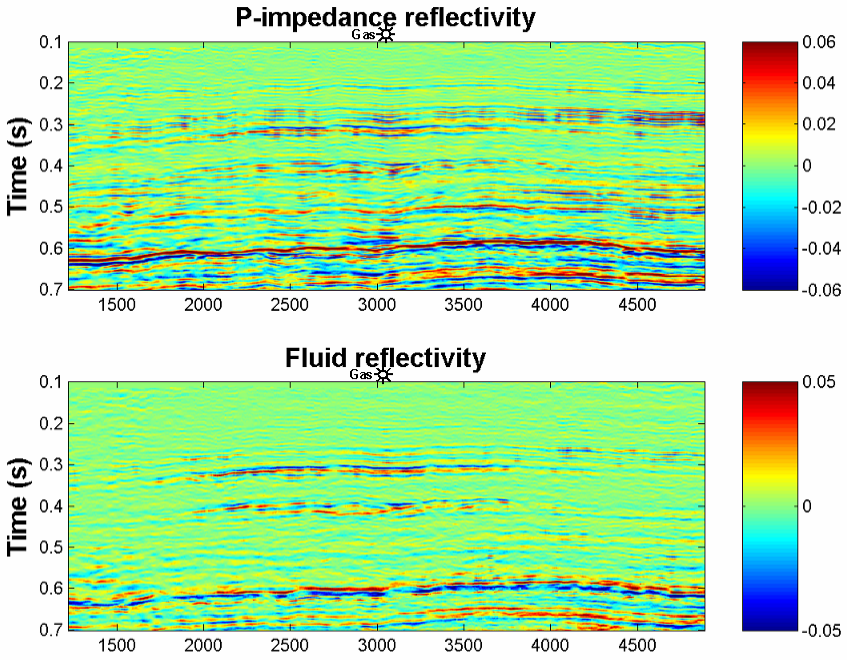

FIG. 9: High-resolution AVO NMO reflectivity inversions. P-wave impedance reflectivity on top and Fluid factor on bottom.

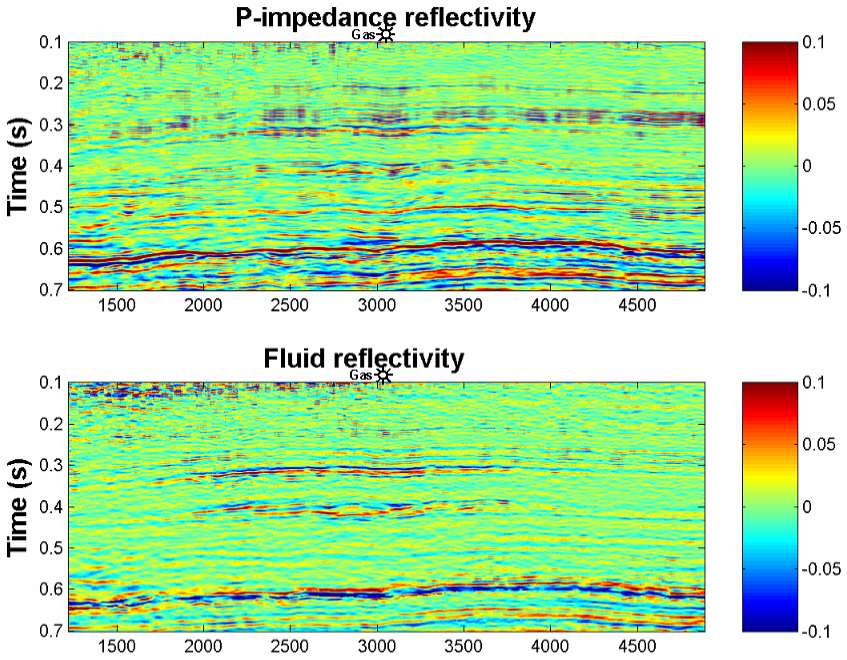

FIG. 10: Traditional AVO NMO reflectivity inversions done on NMO corrected gathers. P-wave impedance reflectivity on top and Fluid factor on bottom.

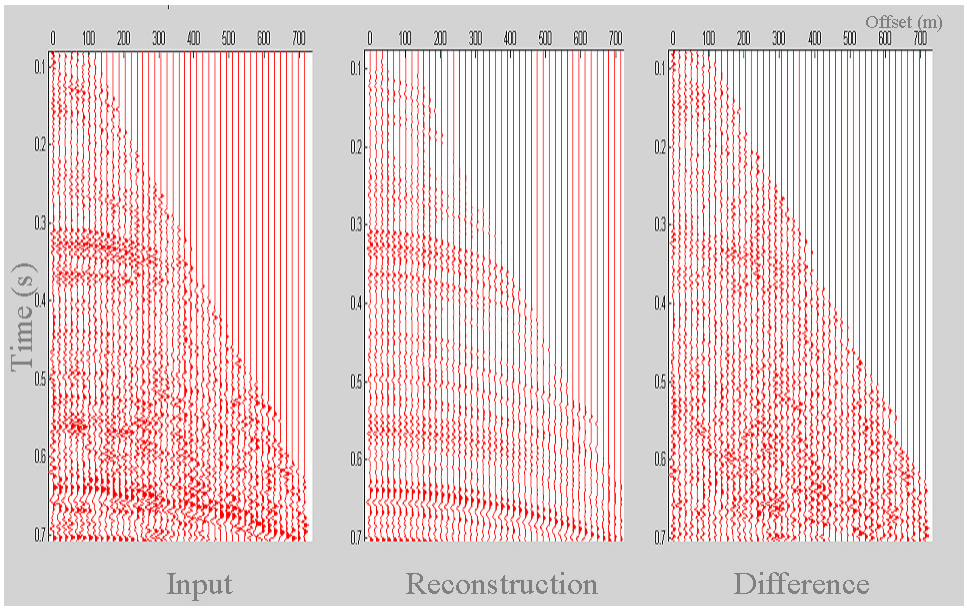

FIG. 11: Input to the AVO NMO inversion (left panel) and the model based on the AVO NMO inversion (middle panel). Note the good match between the two with mostly random noise showing up in the difference (right panel)

IMPEDANCE INVERSION

Rather than outputting reflectivity it is desirable to output impedances. This simplifies the interpretation. However, the seismic data typically is missing low frequencies implying some sort of constraints must be used to get a unique solution. This low frequency trend may be supplied using regional well control and information from an interval velocity travel time inversion from the seismic.

The impedance ξ may be calculated by integrating and taking the exponential of the reflectivity r

$$\xi_k = \xi_0 \exp\left\{2\sum_{n=1}^{N} r_n\right\}. \tag{7}$$

Using this expression it is possible to write a series of constraints that specify that the average estimated impedance from the seismic over some interval must be equal the average impedance of the well log over that same time interval with Σ_w variance

$$\xi_k = \xi_0 \exp\left\{2\sum_{n=1}^{N} r_n\right\}, \tag{8}$$

where $\boldsymbol{P}$ is the linear operator for integration and $\boldsymbol{w}$ is the well log data. This leads to an equation of the form

$$\left[\mathbf{L}^{\mathbf{T}}\mathbf{L} + \mu\mathbf{Q} + \sigma_n^2\mathbf{P}^{\mathbf{T}}\boldsymbol{\Sigma}_w^{-1}\mathbf{P}\right]\mathbf{m} = \mathbf{L}^T\mathbf{d} + \sigma_n^2\mathbf{P}^{\mathbf{T}}\boldsymbol{\Sigma}_w^{-1}\mathbf{w}, \tag{9}$$

which can be solved in a similar fashion to before.

To test this, a simple blocky model was constructed where most reflections follow the mudrock trend. A class III anomaly under going differential tuning was introduced at 1.5 seconds. The reflectivity was generated using the Zoeppritz equation and was convolved with 5/10-40/50 Hz wavelet. Noise was added to give a signal-to-noise ratio of 4. Figure 12 shows the input synthetic gather and the model gather generated by the inversion. Note the excellent match between the two with only random noise showing up in difference display. The reflectivity and impedance estimates are shown in Figure 13. The estimated impedance matches the actual impedance closely even for the tuned class III gas reservoir where one might expect problems.

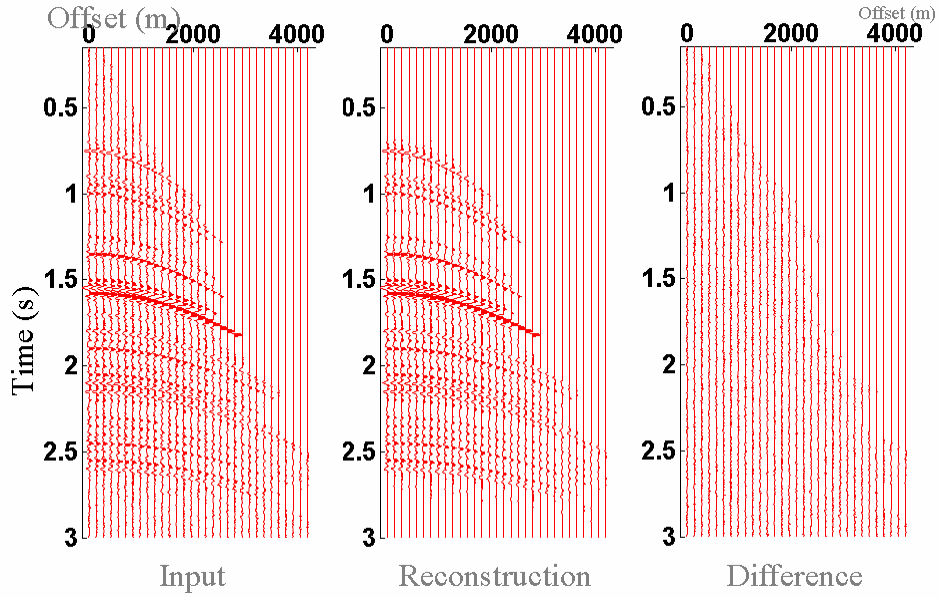

FIG. 12: Input to the high-resolution AVO NMO Impedance inversion (left panel) and the model based on the AVO NMO inversion (middle panel). Note the good match between the two with only random noise showing up in the difference (right panel)

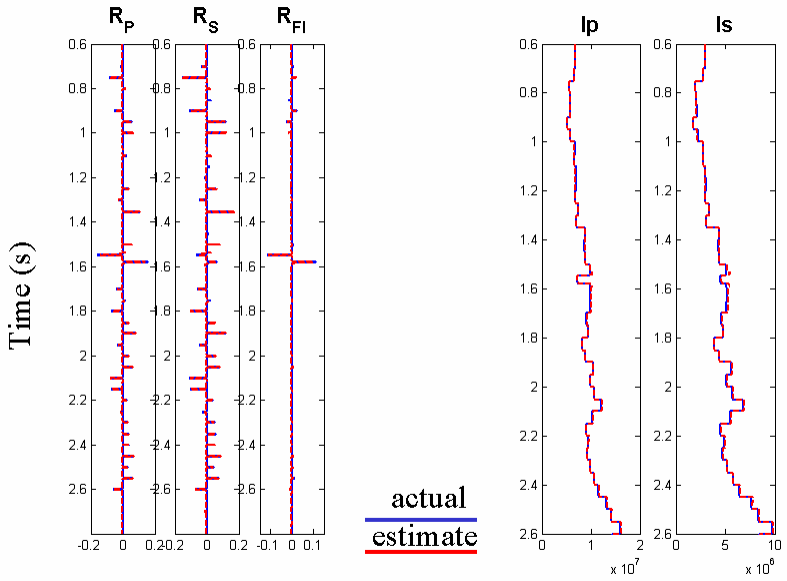

FIG. 13: The right panel shows Fluid factor, P- and S-wave impedance sparse spike reflectivity estimates from the high-resolution AVO NMO Impedance inversion. The estimate is in red while the ideal is in blue. The right hand side shows the reflectivity converted to impedance. Note the excellent match between the estimate and the ideal, even in the tuned class III reservoir.

CONCLUSIONS

High-resolution AVO NMO is better able to resolve reflectors undergoing NMO stretch and differential tuning. This is clearly shown by the synthetic example. The seismic data example shows that high-resolution AVO NMO inversion is more reliable than the estimates provided by the traditional AVO analysis that is performed on a sample-by-sample basis on NMO corrected gathers. This increased reliability is due to the classic trade-off between resolution and stability. A few sparse reflectivity values are estimated with greater certainty than the dense reflectivity at every time sample as in the traditional AVO analysis.

The algorithm is relatively fast. Even though the size of the problem is much larger than the traditional AVO problem, only a few iterations of conjugate gradient are required to come to a satisfactory solution. For the real data example, the algorithm took 8 times as long as the traditional way of solving the problem.

Further by outputting sparse reflectivity, this methodology provides a framework to do elastic impedance inversion similar to poststack sparse spike impedance inversion. The method shown is an extension of poststack sparse spike deconvolution such as presented in Sacchi (1999) or Trad (2002). Comparing this implementation to the poststack implementation, this method has the advantage that the regularization parameter in Equation (4) can be estimated as part of the inversion since the variance of the noise can be estimated from the prestack data. This is not the case for the poststack implementation thus simplifying the implementation. Further by working with prestack data, estimates for both the P- and S-wave impedance reflectivity are possible whereas the poststack case only estimates the P-wave impedance reflectivity.

ACKNOWLEDGEMENTS

The authors would like to thank Core Lab, N.S.E.R.C. and the C.R.E.W.E.S. sponsors for funding this research.

REFERENCES

Dong, W. 1999, AVO detectability against tuning and stretching artifacts: Geophysics, 64, 494-503.

Downton, J. E., Guan, H., and Somerville, R., 2003, NMO, AVO and Stack, 2003 CSPG / CSEG Convention expanded abstracts, http://www.cspgconvention.org/2003abstracts/324s0131.pdf

Downton, J. E. and Lines, L. R., 2002, AVO NMO, 72 Ann. Internat. Mtg., Soc. Expl. Geophys., Expanded Abstracts

Downton, J. E. and Lines, L. R., 2001, AVO feasibility and reliability analysis, CSEG recorder, Vol. 26, No 6, pp 66-73

Fatti, J.L., Smith, G.C., Vail, P.J., Strauss, P.J., and Levitt, P.R., 1994, Detection of gas in sandstone reservoirs using AVO analysis: A 3-D seismic case history using the Geostack technique: Geophysics, 59, 1362-1376.

Hansen, P. H., 1998, Rank-deficient and discrete ill-posed problems: SIAM

Levy, S. and Fullagar, P. K., 1981, Reconstruction of a sparse spike train from a portion of its spectrum and application to high-resolution deconvolution: Geophysics, 46, 1235-1243.

Rutherford, S.,R., and Williams, R.,H., 1989, Amplitude-versus-offset varatiations in gas sands: Geophysics, 54, 680-688

Sacchi, M. D. and Ulrych, T.D., 1995, High-resolution velocity gathers and offset space reconstruction: Geophysics, **60**, 1169-1177.

Sacchi, M. D., 1999, Statistical and transform methods for seismic signal processing, Department of Physics, University of Alberta, available at http://cm-gw.phys.ualberta.ca/~sacchi/saig/publ.html

Sivia, D.S., 1996, Data Analysis, A Bayesian tutorial: Oxford University Press

Shewchuck, J., 1994, An Introduction to the Conjugate Gradient Method Without the Agonizing Pain, School of Computer Science. Carnegie Mellon University. Pittsburg. available at http://www-2.cs.cmu.edu/~jrs/jrspapers.html

Shuey, R.,T., 1985, a simplification of the Zoeppritz equations: Geophysics, **50**, 609-614

Smith, G.,C., and Gidlow, P.,M., 1987, Weighted stacking for rock property estimation and detection of gas: Geophysical Prospecting, **35**, 993-1014

Trad, D., 2002, Implementations and applications of the sparse Radon transform: Ph.D. thesis, University of British Columbia

Walden, A.,T., and White, R.,E., 1984, On errors of fit and accuracy in matching synthetic seismograms and seismic traces; Geophysical Prospecting, **32**, 871-891